

## MEASURING THE METALLICITY OF EARLY-TYPE GALAXIES: (1) COMPOSITE REGION

YU-ZHONG WU

## ABSTRACT

We present the data of 9,739 early-type galaxies (ETGs), cross-matching the Galaxy Zoo 1 with our sample selected from the catalog of the Sloan Digital Sky Survey Data Release 7 of MPA-JHU emission-line measurements. We first investigate the divisor between ETGs with and without star formation (SF), and find the best separator of  $W2-W3=2.0$ . is added. We explore the ETG sample by refusing a variety of ionization sources, and derive 5376 ETGs with SF by utilizing a diagnostic tool of the division line of  $W2 - W3 = 2.0$ . We measure their metallicities with four abundance calibrators. We find that our composite ETG sample has similar distributions of  $M_*$  and star formation rate (SFR) as star-forming galaxies (SFGs) do, that most of them lie on the “main sequence”, and that our fit is a slightly steeper slope than that derived in Renzini & Peng. Compared with the distributions between different metallicities calibrated by four abundance indicators, we find that the Curti17 method is the most accurate calibrator for composite ETGs among the four abundance indicators. We present a weak positive correlation of SFR and metallicity only when the metallicity is calibrated by the PP04, Curti17, and T04 indicators. The correlation is not consistent with the negative correlation of both parameters in SFGs. We suggest that the weak correlation is due to the dilution effect of gas inflow driven by minor mergers.

*Subject headings:* galaxies: early-type — Galaxy: abundances — Galaxy: evolution

## 1. INTRODUCTION

Early-type galaxies (ETGs) are generally thought to be “red and dead” objects, including elliptical and lenticular galaxies, and contain little or no ongoing star formation (SF). Evidence of recent or ongoing SF in ETGs was found by the Galaxy Evolution Explorer (GALEX; Martin et al. 2005). The ultraviolet (UV) measurement provided by the survey is crucial in confirming recent SF (Kaviraj et al. 2009). Yi et al. (2005) and Kaviraj et al. (2007) utilized the Sloan Digital Sky Survey (SDSS) and GALEX survey data to study the ETG sample with UV-optical colors, and showed that the recent low-level SF activity is found in different percentages of their samples.

Growing evidence shows that recent or ongoing SF appears in some ETGs. The SAURON survey can also reveal recent SF in the local ETG sample (Fang et al. 2012). Shapiro et al. (2010) showed that 13 out of 48 SAURON galaxies are classified as “fast rotators” (having a disk component), showing SF activity, while galaxies without ongoing or recent SF are “slow rotators” (spheroidal, Fang et al. 2012). From the morphological category, the slow rotators often are classified as E (elliptical) galaxies, while the fast rotators are S0 (lenticular) galaxies (Emsellem et al. 2007).

For the low-efficiency SF in ETGs, many studies suggest that it is attributed to two mechanisms: internal and external. Internal mechanisms provide energy feedback from SF or active galactic nuclei (AGNs) to suppress SF by heating gas (Cattaneo et al. 2009; Schawinski et al. 2009). External mechanisms contain minor mergers, major mergers, and inflowing of metal-poor gas. Major mergers are more frequent at high redshift, while minor mergers are more usual at low redshift. Minor mergers contribute to SF in nearby ETGs, and Kaviraj

(2014) suggested that the process provides at the least  $\sim 14\%$  of local SF. Belli et al. (2017) found that 9 of 20 quiescent galaxies present evidence of SF activity, and suggested that the low-level activity may be fueled by infalling gas or minor mergers. Direct evidence of gas accretion is an extended ( $\sim 60$  kpc) stellar stream, and Geréb et al. (2016) suggested a merger event in GASS 3505 happening in the recent past.

The gas-phase oxygen abundance (metallicity) is a key fundamental parameter in galaxy formation and evolution, and the metallicity is critical for studying the properties of ETGs. Some studies try to calibrate the metallicity for the H II region of ETGs. Using a sample of quiescent red sequence from the SDSS, Yan (2018) attempted to calibrate the metallicity in galaxies dominated by diffuse ionized gas (DIG)/low-ionization emission region emission, and also presented some puzzles, showing that his results are lower than those calibrated by other metallicity indicators. Utilizing the integral field spectroscopic data of 24 nearby spiral galaxies from the Multi Unit Spectroscopic Explorer, Kumari et al. (2019) obtained the metallicity estimations of the DIG and various galaxies including quiescent galaxies.

In Wu (2020), the optimal division line of  $W2 - W3 > 2.5$  is used as a diagnostic tool to derive the ETG sample with SF, and he measures the metallicities of these ETGs with different abundance calibrators. In this work, we will expand the redshift range to obtain the sample of composite ETGs and explore their properties of these ETGs. Following the selection method of Wu (2020), we obtain the initial ETG sample from the SDSS Data Release 7 (DR7; Abazajian et al. 2009) in Section 2. In Section 3, we first investigate the divisor between ETGs with and without SF with the Wide-field Infrared Survey Explorer (WISE) data (Wright et al. 2010), and then use the separator to derive the ETGs with SF, and to show their properties. We present the metallicities of

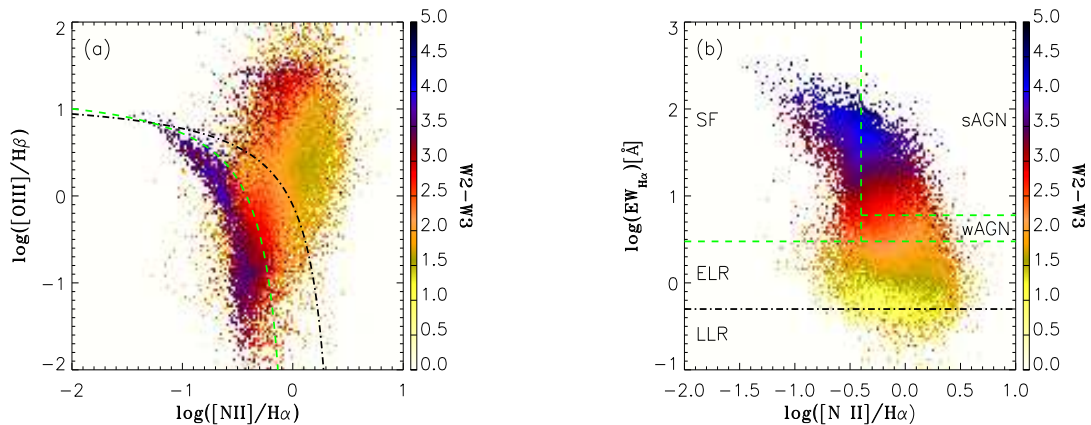


FIG. 1.— (a): BPT diagram; the black dotted-dashed curve is the Kewley (2001) “extreme starburst line” as an upper boundary for SFGs, and the green dashed curve represents the Kauffmann et al. (2003) semi-empirical lower limit for SFGs. (b): WHAN diagram; the spectral classes are described by the green dashed and black dotted-dashed lines.

these ETGs in Section 4. In Section 5, we summarize our results and conclusions.

## 2. THE DATA

Data from SDSS DR7 (Abazajian et al. 2009) are used in this study. The Max Planck Institute for Astrophysics - John Hopkins University (MPA-JHU) SDSS DR7 catalog provides measurements of emission-line fluxes, redshifts, stellar masses, and star formation rates (SFRs) of the SDSS data, which is publicly available<sup>2</sup>. The catalog includes a total of 927,552 galaxy spectra.

Since the SDSS spectra cover a wavelength range of 3800-9200 Å, the lower limit of redshifts in our sample is  $z \approx 0.023$ , and this ensures that the  $[\text{O II}]\lambda\lambda 3227, 3229$  can appear in the observed range (Wu & Zhang 2013). 0.2 is used as the upper limit of redshifts in our study, and the redshift limit can avoid K-corrections of the WISE data (Herpich et al. 2016). The aperture-covering fractions are calculated from the fiber and Petrosian magnitudes in the r-band, and the fractions are  $> 20\%$  for our galaxies. Following the method of Wu (2020), we choose galaxies with a signal-to-noise ratio (S/N)  $> 2$  for  $[\text{O II}]\lambda\lambda 3227, 3229$ , and  $[\text{N II}]\lambda 6584$ , and with  $\text{S/N} > 3$  for  $\text{H}\alpha$  and  $\text{H}\beta$ . In addition, the status of the SFR measurements is shown by an SFR FLAG keyword, and the keyword is required to be zero. As a result, our initial sample has 221,861 galaxies.

With regard to ETGs, two judgment criteria must be satisfied (Wu 2020). The first one is that these galaxies should be  $n_{\text{Sersic}} > 2.5$ , and the second one is the elliptical probability ( $p$ ) of more than 0.5 (Herpich et al. 2018). All probabilities are derived following the debiased procedure in this work. Here, the Sérsic index is provided by the New York University Value-Added Galaxy Catalog<sup>3</sup> (NYU-VAGC; Blanton et al. 2005). Moreover, Galaxy Zoo 1 (Lintott et al. 2008, 2011) is used to be the standard for our galaxy morphologies by matching our sample with that found in Table 2 of Lintott et al. (2011). We first cross-match our initial sample with the NYU-VAGC within  $2''$ , and select these galaxies with

$n_{\text{Sersic}} > 2.5$ . Then we choose the galaxies with  $p > 0.5$  (Herpich et al. 2018), and match our galaxies with Table 2 of Lintott et al. (2011) within  $2''$ . Wu (2020, in preparation) employed the debiased elliptical probabilities of  $p > 0.5$  and  $p > 0.8$  to obtain the two composite ETG samples, and found that the two ETG samples have similar distributions and median values of stellar mass, specific star formation rate (sSFR;  $\text{sSFR} = \text{SFR}/M_*$ ), u-r color, and equivalent width of  $\text{H}\alpha$ . In this study, we also utilize the probability of  $p > 0.5$  to select our ETGs. We then obtain 26,630 galaxies.

In this study, we consider these ETGs, which are located in the composite region on the Baldwin-Philips-Terevich (BPT) diagram (Baldwin et al. 1981). Because SF and AGN activities may coexist in these galaxies, we need to assess the contributions of SF and AGN on photoionization in those galaxies. Kewley et al. (2001, 2006) utilized models and built an extreme starburst line, an upper limit on the emission-line strengths in star-forming galaxies (SFGs). This indicates that these galaxies that lie below the curve are dominated by SF (Griffith et al. 2019), so we need only to study these galaxies locating in the composite region on the BPT diagram in this study. Our sample then includes 9,739 composite galaxies.

In Wu (2020),  $W2-W3=2.5$  is used to distinguish between SF and non-SF photoionization mechanisms in composite ETGs. Here W2 and W3 come from WISE (Wright et al. 2010), and the survey covers the whole sky in four bands: W1, W2, W3, and W4, corresponding to their central wavelengths of 3.4, 4.6, 12, and 22  $\mu\text{m}$ , respectively. The catalog provides the accurate position, four-band fluxes, their instrumental profile-fit photometry magnitudes, and their instrumental profile-fit photometry S/N ratios, and it is publicly available<sup>4</sup>. The above-mentioned ETG sample is cross-matched by using the AllWISE source catalog within  $2''$ , and then those ETGs with  $\text{S/N} > 3$  for W2 and W3 are selected. Finally, we have a sample of 6,978 ETGs.

In this study, the measurements of  $M_*$  and SFRs are corrected using a Chabrier (2003) initial mass function (IMF) from a Kroupa (2001) IMF assumed in the MPA-

<sup>2</sup> <https://www.mpa.mpa-garching.mpg.de/SDSS/DR7/>

<sup>3</sup> <http://sdss.physics.nyu.edu/vagc-dr7/vagc2/sersic/>

<sup>4</sup> <https://irsa.ipac.caltech.edu/cgi-bin/Gator/nph-dd>

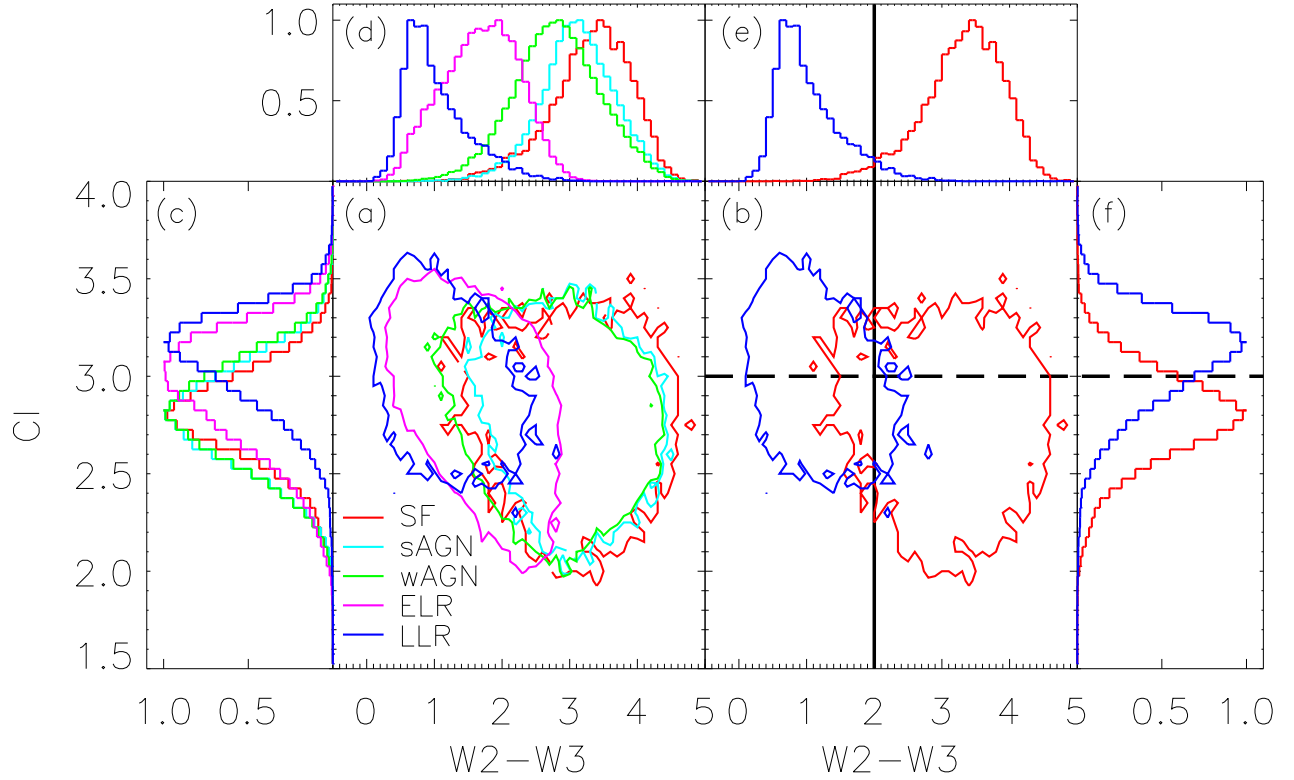


FIG. 2.— (a): The distribution of the WHAN classes in the W2-W3 vs. CI diagram. The contours include the 95% distributions of all selected ETGs for each WHAN class, shown in the legend. (d): Histograms for the WHAN spectral classes for the W2-W3 color. All the histograms are normalized by the peak of their corresponding distribution in this figure. (c): Same as (d) for the CI parameter. (b), (e), and (f) are the same as (a), (d), and (c), respectively, but only for SF ETGs and LLR ETGs, with the black solid line indicating the best divisor between the absence and presence of SF ( $W2-W3=2.0$ ), and the black dashed line representing the best divisor between SF ETGs and LLR ETGs with respect to the concentration index ( $CI=3.0$ ).

TABLE 1  
SAMPLE OF COMPOSITE EARLY-TYPE GALAXIES.

R.A. (J2000)	Decl. (J2000)	Redshift	$\log(M_*)$ $M_\odot$	$\log(\text{SFR})$ $M_\odot/\text{yr}$	frac <sup>a</sup>	P <sup>b</sup>	$12 + \log(\text{O}/\text{H})$			
							PP04	T04	Jon15	Curtil7
(1)	(2)	(3)	(4)	(5)	(6)	(7)	(8)	(9)	(10)	(11)
01:45:52.6	14:30:54.0	0.20	11.22	1.08	0.31	0.54	$8.78 \pm 0.02$	$9.13 \pm 0.02$	$8.53 \pm 0.03$	$8.75 \pm 0.02$
14:48:56.9	23:58:08.4	0.12	10.86	0.49	0.43	0.80	$8.76 \pm 0.03$	$9.12 \pm 0.03$	$8.50 \pm 0.05$	$8.71 \pm 0.02$
03:56:29.8	-05:40:30.0	0.06	9.99	-0.29	0.42	0.63	$8.50 \pm 0.01$	$8.72 \pm 0.03$	$8.40 \pm 0.01$	$8.47 \pm 0.01$
00:40:04.2	-00:34:12.9	0.11	10.78	0.77	0.42	0.75	$8.63 \pm 0.02$	$9.05 \pm 0.03$	$8.33 \pm 0.05$	$8.64 \pm 0.02$
08:09:10.3	08:17:58.7	0.05	10.64	-0.22	0.26	0.62	$8.66 \pm 0.01$	$8.89 \pm 0.03$	$8.56 \pm 0.02$	$8.61 \pm 0.01$
14:50:27.4	30:29:11.4	0.05	10.12	-0.12	0.43	0.64	$8.51 \pm 0.01$	$8.69 \pm 0.02$	$8.32 \pm 0.01$	$8.42 \pm 0.01$
13:37:17.0	32:15:16.2	0.06	10.35	0.40	0.39	0.67	$8.71 \pm 0.02$	$8.95 \pm 0.04$	$8.54 \pm 0.04$	$8.65 \pm 0.02$
09:46:47.5	09:03:56.3	0.06	10.31	-0.84	0.45	0.64	$8.55 \pm 0.06$	$8.51 \pm 0.28$	$8.64 \pm 0.06$	$8.52 \pm 0.07$
13:28:53.8	01:58:25.2	0.14	10.73	-0.50	0.36	0.59	$8.74 \pm 0.10$	$8.90 \pm 0.13$	$8.58 \pm 0.14$	$8.66 \pm 0.10$
04:04:10.9	-05:38:09.0	0.07	10.19	-0.79	0.33	0.52	$8.39 \pm 0.00$	$8.67 \pm 0.01$	$8.28 \pm 0.01$	$8.42 \pm 0.01$
...	...	...	...	...	...	...	...	...	...	...

NOTE: <sup>a</sup> Values were calculated from the fiber flux and petro flux ratio. <sup>b</sup> represent the elliptical probability following the debiasing procedure.

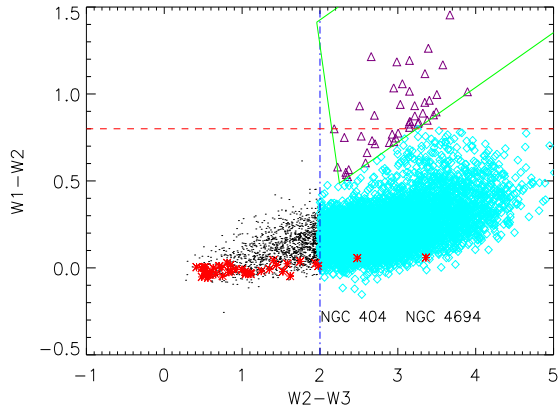


FIG. 3.—  $W2-W3$  vs.  $W1-W2$  color-color diagram for composite ETGs. The best boundary between ongoing SF and retired galaxies is displayed by the blue vertical dotted-dashed line. The mid-infrared standard is shown by the red horizontal dashed line to choose AGNs suggested by Stern et al. (2012). The “AGN” wedge suggested by Mateos et al. (2012) is shown by the green solid lines. The cyan diamonds are our final sample with star formation. The purple triangles and black dots are composite ETGs with AGNs and without SF, respectively. These ETGs with metallicity measurements are shown by the red asterisks, and these measurements come from Athey & Bregman (2009), Annibali et al. (2010), Bresolin 2013, and Griffith et al. (2019).

JHU catalog. The gas-phase oxygen abundances in SFGs are calibrated by different metallicity estimators based on various H II region models. In ETGs, there are many ionization sources, for example, SF, AGN activities, cosmic rays, shocks, and old, hot stars, Griffith et al. (2019) estimated the metallicities of three ETGs by excluding those ionization sources, which influence the metallicity measurements. Brown et al. (2016) compared the performance of several metallicity indicators in 200,000 SFGs, and concluded that the PP04-O3N2 (PP04; Pettini & Pagel 2004) indicator is suggested as the most perfect calibrator. In this study, we also calibrate the metallicity of ETGs with O3N2 from Pettini & Pagel (2004), R23 from Tremonti et al. (2004, T04), O32 from Jones et al. (2015, Jon15), and O3S2 from Curti et al. (2017, Curti17).

### 3. DEFINITION AND PROPERTIES OF THE ETG SAMPLE

In Wu (2020), based on using extragalactic H II regions and photoionization models to measure the metallicity of composite ETGs, a sample of 2,218 ETGs was obtained. Based on the sample from Wu (2020), we will present herein the sample of composite ETGs by relaxing the redshift range. On the basis of the expanding sample, we also study the properties of various parameters in this composite ETG sample.

#### 3.1. WISE division between star-forming ETGs and lineless retired ETGs

In Herpich et al. (2016), the SDSS DR7 and WISE data are used together to establish the divisor between galaxies with and without SF, a mid-infrared color  $W2-W3=2.5$ . The mid-infrared separator is based on a sample of galaxies of all morphological types, and in this section we will construct a separator to separate ETGs with and without SF. In Cluver et al. (2014), the  $W2-W3$  vs.

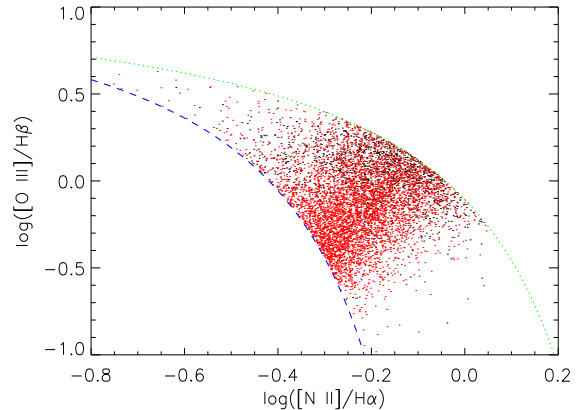


FIG. 4.— BPT diagnostic diagram. The black and red dots represent composite ETGs without and with SF, respectively. The green dotted and blue dashed curves show the Kewley et al. (2001) “extreme starburst line” and Kauffmann et al. (2003) SFG lower limit, respectively.

$W1-W2$  diagram shows the location of different kinds of objects, and presents the finding that some sources dominated by SF have  $W2-W3 > 1.5$  Vega magnitudes. Here, we use the method from Herpich et al. (2016) to explore the separator between ETGs with and without SF.

Based on the classification scheme of Cid Fernandes et al. (2011), for SFGs,  $\log([N II]/H\alpha) < -0.4$  and  $EW_{H\alpha} > 3\text{\AA}$ ; for strong AGNs,  $\log([N II]/H\alpha) > -0.4$  and  $EW_{H\alpha} > 6\text{\AA}$ ; for weak AGNs,  $\log([N II]/H\alpha) > -0.4$  and  $3\text{\AA} < EW_{H\alpha} < 6\text{\AA}$ . Those galaxies with  $EW_{H\alpha} < 3\text{\AA}$  are suggested to be retired galaxies, showing that these sources stopped forming stars long ago and their ionizing mechanism is dominated by hot low-mass evolved stars (Herpich et al. 2016). In addition, emission lines have not been detected in some of them. Therefore, this type of galaxies can be classified into two categories: with and without emission lines. The sources with  $EW_{H\alpha} < 0.5\text{\AA}$  are suggested as “lineless retired” (LLR) galaxies, and another sources with  $0.5\text{\AA} < EW_{H\alpha} < 3\text{\AA}$  are “emission-line retired” (ELR) galaxies (Cid Fernandes et al. 2011; Herpich et al. 2016). On the basis of the method from Herpich et al. (2016), their SFGs, strong AGNs, weak AGNs, ELR galaxies, and LLR galaxies correspond to our SF ETGs, strong AGN ETGs, weak AGN ETGs, ELR ETGs, and LLR ETGs, respectively, and the five types of ETGs are categorized in the  $EW_{H\alpha}$  vs.  $[N II]/H\alpha$  (WHAN) diagram.

For the five galaxy categories, we employ the Herpich et al. (2016) method to explore the divisor between ETGs with and without SF. First, we require  $S/N > 3$  for  $H\alpha$  and  $[N II]$  for them but no LLR galaxies. Moreover,  $n_{Sersic} > 2.5$  and  $p > 0.5$  ( $p$  is the elliptical probability following the debiased procedure) are considered to select ETGs with five types of ETGs, and we obtain 137,066 ETGs. Because the WISE data are used in Figure 1,  $S/N > 3$  for  $W2$  and  $W3$  are required, and finally 72,343 ETGs with the  $W2-W3$  color bars are shown in Figure 1. In Figure 1(a), the green dashed and black dotted-dashed curves represent the Kauffmann et al. (2003) semi-empirical lower limit and the Kewley et al. (2001) theoretical extreme starburst line upper boundary for

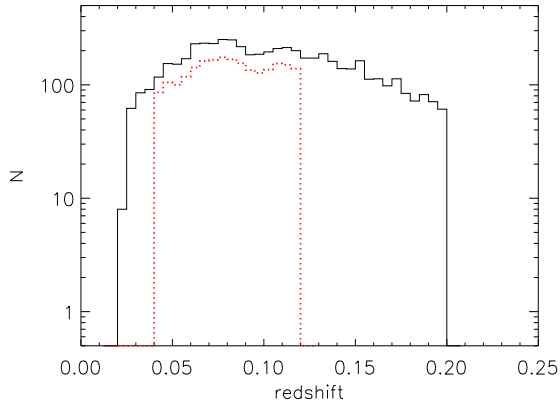


FIG. 5.— Distributions of redshift for composite ETGs. The red dotted and black lines describe the sample of composite ETGs with  $0.04 < z < 0.12$  and  $0.023 < z < 0.2$ , respectively.

SFGs. We find that ETGs located in the H II region have a larger W2-W3 color than ones located in the composite and AGN regions, and that some ETGs lying in the AGN region at  $\log([\text{N II}]/\text{H}\alpha) \sim -0.3$  and  $\log([\text{O III}]/\text{H}\beta) \sim 1.3$  also present larger W2-W3 colors.

In Figure 1(b), we use the green dashed and dotted-dashed lines to delimit the five types of ETGs: SF, sAGN, wAGN, ELR, and LLR ETGs, which correspond to star-forming ETGs, strong AGN ETGs, weak AGN ETGs, ETGs with  $0.5\text{\AA} < \text{EW}_{\text{H}\alpha} < 3\text{\AA}$ , and ETGs with  $\text{EW}_{\text{H}\alpha} < 0.5\text{\AA}$ , respectively. Figure 1(b) shows 6,873 star-forming ETGs, 17,929 sAGN ETGs, 12,047 wAGN ETGs, 34,230 ELR ETGs, and 1,264 LLR ETGs. Compared with Figure 1 of Herpich et al. (2016), star-forming ETGs have a smaller sample, while ELR ETGs have a larger sample. We will expand the sample of SF ETGs by excluding the demand of  $\text{S/N} > 3$  for the [N II] line.

For SF and LLR ETGs, we use  $\text{S/N} > 3$  for H $\alpha$  and [N II] to obtain 6,873 and 1,264 sources, respectively. With regard to the small number of LLR ETGs, this is because LLR ETGs do not often have emission lines, and therefore here we only use  $\text{S/N} > 3$  for H $\alpha$  to choose LLR ETGs. Utilizing  $n_{\text{Sersic}} > 2.5$ ,  $p > 0.5$ , and  $\text{S/N} > 3$  for W2 and W3 conditions, we finally obtain 6,397 LLR ETGs. In Figure 2, we present the distributions of the five types of ETGs in the W2-W3 vs. concentration index (CI) diagram. CI is defined as  $R_{90}/R_{50}$ , and  $R_{90}$  and  $R_{50}$  is the radius including 90% and 50% of the Petrosian flux, respectively. The data of star-forming, sAGN, wAGN, ELR ETGs from Figure 1, and the data of LLR ETGs from 6,397 sources are shown in Figure 2.

In Figure 2(a), we use 77,476 ETGs to describe the distributions of the five types of ETGs in the W2-W3 and CI diagram. The contours with the red, cyan, green, magenta, and blue colors correspond to the star-forming, sAGN, wAGN, ELR, and LLR ETGs, respectively. From Figure 2(d), we can see that the W2-W3 color decreases basically along the SF-sAGN-wAGN-ELR-LLR order. The W2-W3 sequence is in the similar CI as Figure 2(c), and the result has been observed in Cid Fernander et al. (2011) and Herpich et al. (2016). Following a similar method to Herpich et al. (2016), the star-forming and LLR ETGs, located at opposite ends of Figure 2(a),

are used to decide the best W2-W3 separator between ETGs with and without SF. The LLR inconsistency between the W2-W3 color and emission lines, indicating SF and galaxy retirement, respectively, can be explained by these objects being galaxies with SF disks having the old “retired” bulge, which is covered by the SDSS fibre (Herpich et al. 2016). This indicates that 3” fiber spectra show their old and retired bulges, and that the WISE emission presents the SF disk.

We also employ the method of Strateva et al. (2001) and show the definitions of the completeness and the reliability. The best separator is derived by maximizing the parameter  $P = C_{\text{SF}}R_{\text{SF}}C_{\text{LLR}}R_{\text{LLR}}$  (Herpich et al. 2016), which has been done by Strateva et al. (2001), Mateus et al. (2006), Cid Fernandes et al. (2011), and Herpich et al. (2016). We have  $\text{CI}=3.0$ , which is the optimal divisor between LLR ETGs and star-forming ETGs.  $\text{CI}=2.63$ , 2.62, and 2.75 were found in Strateva et al. (2001), Mateus et al. (2006), and Herpich et al. (2016). In Figures 2(b) and 2(f), we show the value with a black dashed line. Following the same method to apply the WISE color, we have obtained the best divisor between ETGs with and without SF, W2-W3=2.0 mag, described by the black vertical solid line in Figure 2(b) and 2(e). The value is 0.5 mag smaller than that proposed by Herpich et al. (2016), and our value can be explained because the value of W2-W3=2.5 is suitable for all galaxy methodologies in Herpich et al. (2016), while our value is applied to all ETGs, for example, wAGN ETGs, LLR ETGs, and ELR ETGs, generally having a smaller W2-W3 color.

### 3.2. The Sample of Composite ETGs

In SFGs, gas-phase oxygen abundances are estimated by using various calibrators, which are all based on extragalactic H II regions and photoionization models. In ETGs, we still utilize these metallicity calibrators to calculate the metallicity of ETGs, and we require some ETGs to satisfy the same or similar conditions as SFGs. With regard to SFGs and ETGs, an ionization source difference between two types of galaxies is significant, and the former ones contain only SF, while the latter ones may include many other ionization sources, AGN activities, shocks, cosmic rays, and asymptotic giant branch (PAGB), for example (Griffith et al. 2019). Therefore, we need an evaluation for various possible ionization sources in ETGs.

In this work, we can exclude a photoionization mechanism of AGN activities because our ETG sample locates in the composite region on the BPT diagram, and it is dominated by SF activity (Griffith et al. 2019). Following the method of Wu (2020), we also ignore the shock excitation mechanism. Based on the suggestion by Sparks et al. (1989) concerning typical velocities and densities, the shock energy is too low by 100 times (Athey & Bregman 2009). Also, the two ionization sources, extra heat or cosmic ray, are excluded, because the line flux ratio excited by galaxies located in the composite or AGN regions on the BPT diagram is far larger than that excited by the two sources in Figure 4 of Griffith et al. (2019). Moreover, PAGB stars provide energy of the same order of magnitude as weak AGNs, and are suggested as a photoionization source; therefore, many galaxies are actually dominated by SF, however they are misclassified as active

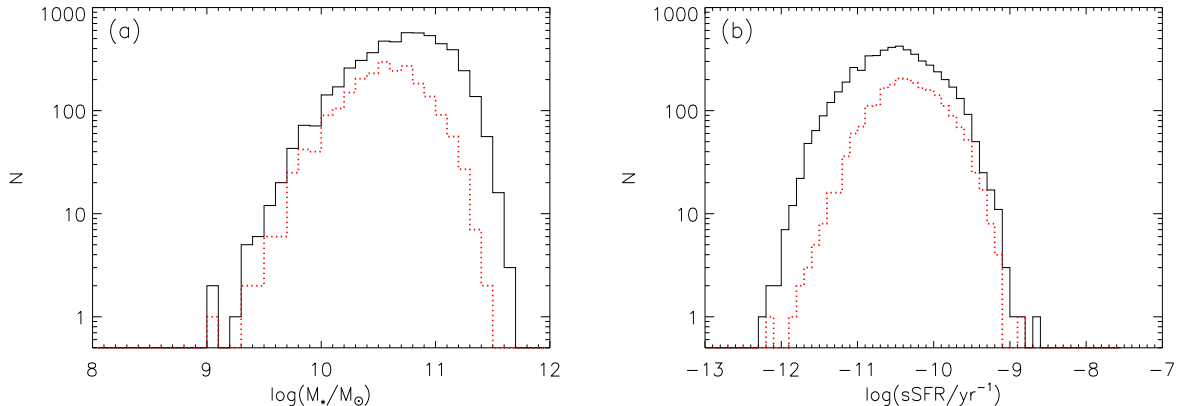


FIG. 6.— Comparison of stellar mass (left) and sSFR (right) distributions for composite ETGs. The red dotted and black lines are the same as in Figure 5.

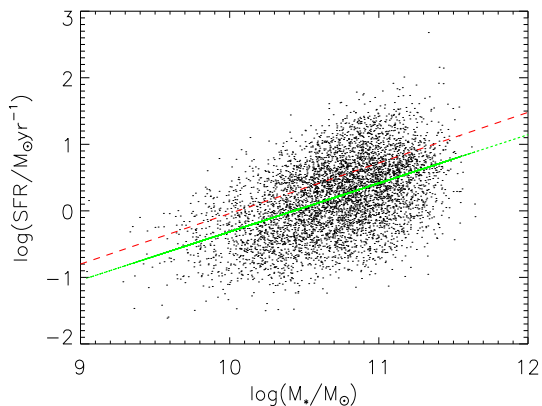


FIG. 7.— Stellar mass vs. SFR for the composite ETG sample. The green solid and red dashed lines are the best fits of this study and Renzini & Peng (2015) for their corresponding data, respectively.

galaxies (Belfiore et al. 2016).

In Athey & Bregman (2009), the  $[\text{Ne III}]\lambda 3869$  line is suggested as a key index of collisional excitation, and  $[\text{Ne III}]\lambda 3869$  fluxes appear in NGC 4125 and NGC 2768, therefore six objects are removed from their sample. In our ETG sample, we exclude four sources, and 6,974 ETGs remain. Also, we need to remove an excitation mechanism, single-degenerate (SD) Type Ia supernovae progenitors (Woods & Gilfanov 2014). A diagnostic diagram of  $[\text{O I}]\lambda 6300/\text{H}\alpha$  versus  $[\text{O III}]\lambda 5007/\text{H}\beta$  was introduced by Griffith et al. (2019) to remove the ionization mechanism, and the threshold of  $[\text{O I}]\lambda 6300/\text{H}\alpha \sim 0.5$  was applied to the comparison of emission-line ratios in those samples of Athey & Bregman (2009), Annibali et al. (2010), Griffith et al. (2019), and Wu (2020). So, we obtain 6,789 ETGs.

In Wu (2020), the relation between  $W2-W3$  and  $W1-W2$  for composite ETGs was shown. Here, we also employ the method to obtain those ETGs with photoionization excited by SF. In Figure 3, we display the similar figure to Figure 3 from Wu (2020). The line of  $W2-W3 = 2.5$  is suggested as the best dividing line between galaxies with and without SF (Herpich et al. 2016), and the line

demonstrates the important potential for distinguish between ETGs dominated by SF and non SF (Wu 2020). Here, we use the line of  $W2-W3 = 2.0$  to obtain ETGs dominated by SF. The red dashed line of  $W1-W2 = 0.8$  is suggested as the mid-infrared criterion proposed by Stern et al. (2012) to discriminate galaxies with nuclear activity from those no nuclear activity in Figure 3, and the measurements of  $W1-W2 > 0.8$  indicate that almost all infrared emission comes from nuclear activity (Caccianiga et al. 2015). Also, the green lines are suggested as the demarcation between galaxies with and without nuclear activity (Mateos et al. 2012), and the purple triangles located in the “AGN” wedge show 46 ETGs with nuclear activity.

After the exclusion of ETGs with nuclear activity, we consider those ETGs with SF. Composite ETGs without SF are shown as the black dots in Figure 3, and they are located to the left of the blue dotted-dashed line of  $W2-W3 = 2.0$ , finding 1,353 ETGs. Moreover, those ETGs with metallicity measurement, displayed by red asterisks, come from Athey & Bregman (2009), Annibali et al. (2010), Bresolin (2013), and Griffith et al. (2019). One of these ETGs, located to the right of the blue dotted-dashed line of Figure 3, is NGC 4694, and this galaxy lies in the H II region on the BPT diagram (Griffith et al. 2019), belonging to star-forming ETGs (these ETGs are located in the H II region in the BPT diagram, Wu et al. 2020, in preparation). Another one of these ETGs, marked it as “NGC 404” in Figure 3, is the nearby S0 galaxy with extended SF (Bresolin 2013). The cyan diamonds in Figure 3, which have  $W2-W3 > 2.0$ , are composite ETGs with SF, and they indicate that a dominant photoionization source comes from SF in these ETGs (Wu 2020). We finally derive the sample of 5,376 ETGs, increasing by 142% relative to the ETG sample of Wu (2020).

These composite ETGs are displayed in Figure 4. The ETGs in Figure 4 have a similar distribution to Figure 1 of Wu (2020). As can be seen in Figure 4, most of the red and the black dots approach the blue dashed curve and the green dotted curve, respectively (Wu 2020). In Table. 1, we provide various parameters of composite ETGs. R.A, Decl, redshift, stellar masses, SFRs, the fiber and petro flux ratio (frac), and p (the debiased el-

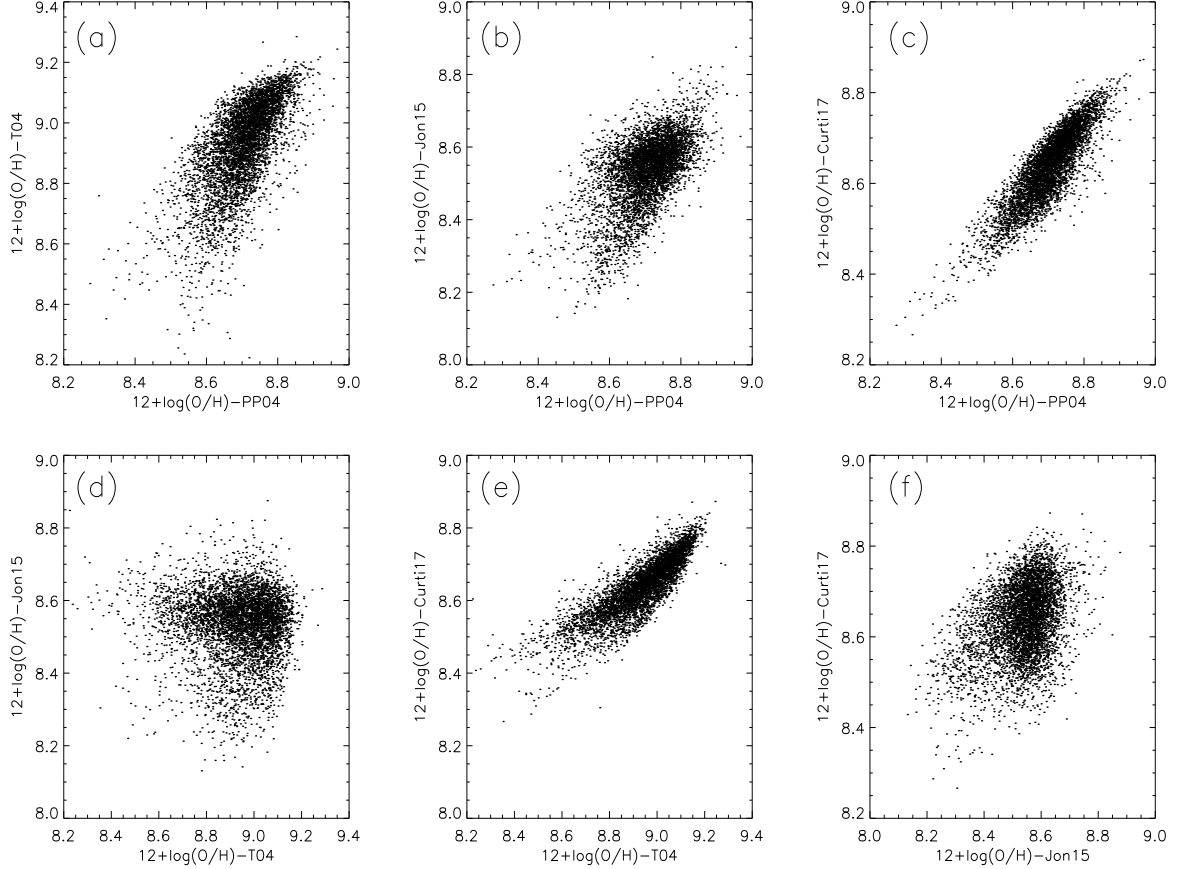


FIG. 8.— Comparison between metallicities calibrated by different abundance indicators for composite ETGs.

liptical probability) for these ETGs are selected from the MPA-JHU catalog. The four kinds of metallicities are calibrated by the PP04, T04, Jon15, and Curti17 abundance indicators, respectively.

### 3.3. Sample Properties of Composite ETGs

In Wu (2020), some detailed properties of the composite ETG sample were not demonstrated. Here, we will display them. Compared with the sample from Wu (2020), the sample of ETGs is expanded to a redshift range of  $0.023 - 0.2$ , having a median value of  $\sim 0.10$ . In Figure 5, we show the redshift distributions of the ETG samples. The red dotted lines represent the distribution of ETGs with  $0.04 < z < 0.12$ , while the black lines show the distribution of ETGs with  $0.023 < z < 0.2$ . The ETG sample of Wu (2020) accounts for  $\sim 41\%$  of our ETGs.

In Figure 6(a), we show the distributions of stellar mass for the ETG samples, and the red dotted and black lines are the distributions of ETGs with  $0.04 < z < 0.12$  and  $0.023 < z < 0.2$ , respectively. From Figure 6(a), the ETG sample of  $0.04 < z < 0.12$  occupies mainly the lower stellar mass section of the ETG sample of  $0.023 < z < 0.2$ . In Wu (2020), the sample of composite ETGs is mainly distributed at  $10.0 < \log(M_*/M_\odot) < 11.0$ , which accounts for 86% of the whole sample. With the redshift range increasing,  $10.0 < \log(M_*/M_\odot) < 11.5$  is the main distribution range of our ETG sample, occupying  $\sim 95\%$  of our sample. The median values of stellar masses of

the two ETG samples are  $\sim 10.58$  and  $10.75$ , respectively. These indicate that some ETGs with a lower stellar mass may have emission lines that are too weak to be observed in the SDSS data.

Figure 6(b) shows the distributions of sSFR for the ETG samples. The sSFR distributions of our ETG sample and the sample from Wu (2020) have a similar range, from  $\log(\text{sSFR}) \sim -11.0$  to  $\sim -9.5$ , accounting for 80% of our whole composite ETG sample, and their median values are  $-10.50 \text{ yr}^{-1}$  and  $-10.34 \text{ yr}^{-1}$ , respectively. Compared to the sSFR distribution of star-forming ETGs, our distribution has almost the same sSFR range as theirs, except  $\log(\text{sSFR}) \sim -8.0$  for star-forming ETGs (Wu et al. 2020, in preparation). These indicate that our composite ETG sample has a similar SF capability as star-forming ETGs, located in the H II region on the BPT diagram. In the meantime, these imply that the photoionization source of our composite ETGs is dominated by SF.

Figure 7 gives an overview of the distribution of  $M_*$  and SFR in our composite ETG sample. We find that the distribution of our ETG sample is similar to the SFG one, and most of our composite ETG sample lies on the “main sequence” (Noeske et al. 2007; Salim et al. 2007; Renzini & Peng 2015), but our sample is lower than the main sequence by 0.2-0.3 dex. The green solid line in Figure 7 is the best least-squares fits for our composite ETG sample, and the fit is  $\log(\text{SFR}) = (0.73 \pm 0.02)\log(M_*/M_\odot) - 7.61 \pm 0.19$ , with a slightly

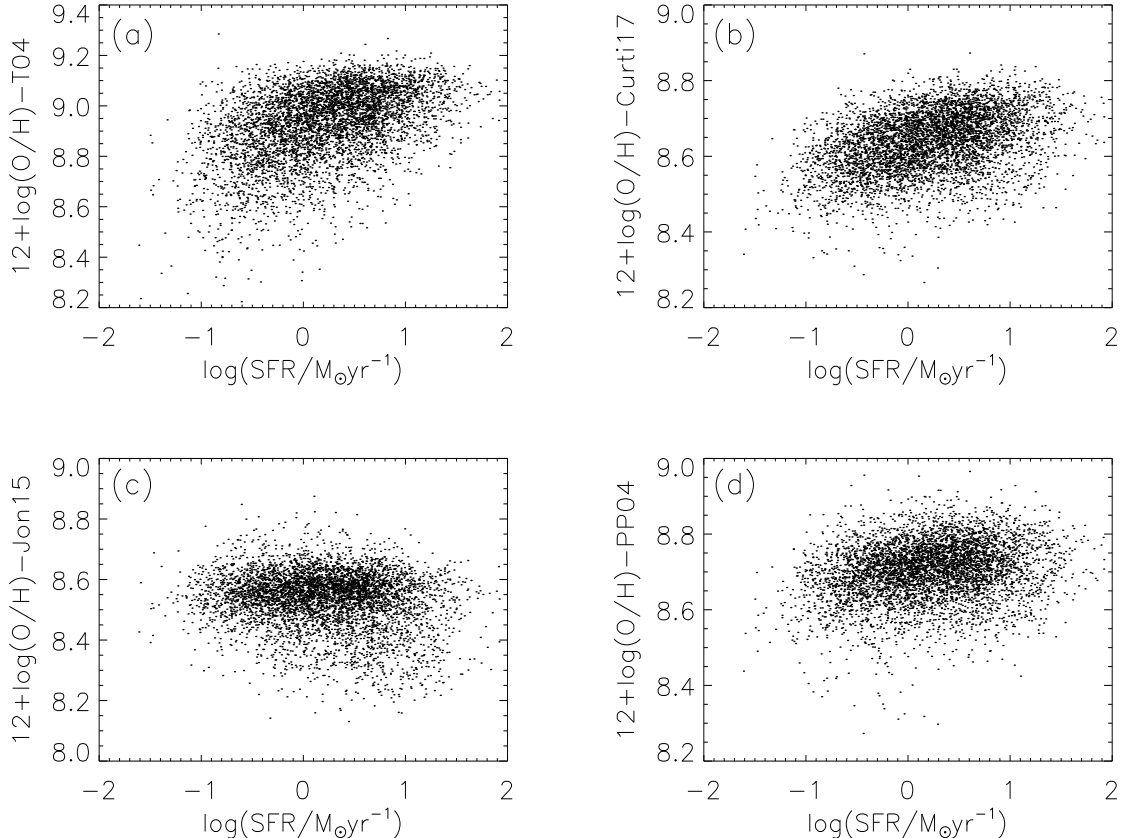


FIG. 9.— Comparison of the distributions of SFR and metallicity for composite ETGs, and these metallicities are estimated by the T04, Curti17, Jon15, and PP04 metallicity indicators, respectively.

flatter slope than obtained in Renzini & Peng (2015), which was  $0.76 \pm 0.01$ . For reference, the main sequence for the SDSS data at  $z \sim 0$  from Renzini & Peng (2015) is described by the red dashed line in Figure 7. The main sequence of SFGs is one of the most important relations in galaxy evolution, and the tight correlation is confirmed by many studies. The figure demonstrates a significant trend for lower/higher  $M_*$  galaxies to have a lower/higher SFR. They have a correlation, with the Spearman coefficient  $r=0.47$ .

#### 4. METALLICITIES OF THE ETG SAMPLE

Wu (2020) measured the metallicities of composite ETGs with six abundance indicators, and found that two calibrators can not estimate the metallicity of ETGs. Here, we will use another four metallicity estimators to study the metallicity properties of composite ETGs. Besides the PP04 estimator, we also utilize the metallicity indicators of R23 of T04, O32 of Jon15, and O3S2 of Curti17, respectively. In the Curti17 indicator, we use Equation (7) of Kumari et al. (2019):  $O3S2 = -0.046 - 2.223X_{O3S2} - 1.073(X_{O3S2})^2 + 0.534(X_{O3S2})^3$ , where  $x_{O3S2}$  represents oxygen abundance, which is normalized to the solar value in the form  $12 + \log(O/H)_{\odot} = 8.69$ . In the third-order polynomial for  $x_{O3S2}$ , we utilize the IDL function of `fz_roots` to calculate a real root of  $x_{O3S2}$ .

In Figure 8, we show the distributions between metallicities calibrated by four abundance indicators. Through

these comparisons between these metallicities, the best metallicity calibrator for our ETGs can be identified among the four abundance estimators. In Figure 8(a), we show the relation between metallicities calibrated by PP04 and T04 calibrators, and their correlation is significant, showing the Spearman coefficient  $r=0.68$ . In Figure 8(b), the correlation between PP04 and Jon15 calibration metallicities slightly decreases, presenting a Spearman coefficient  $r=0.55$ . In Figure 8(c), the correlation between PP04 and Curti17 estimation metallicities displays the best one among all these relations, exhibiting the Spearman coefficient  $r=0.84$ . Using Figures 8(a)-(c), we can see that the Curti17 calibrators are better indicators than the T04 and Jon15 ones, and the T04 indicator may be a better calibrator than the Jon15 one.

In Figure 8(d), we demonstrate the relation between metallicities calibrated by the T04 and Jon15 estimators. Their relation is significantly unordered, and it does not present a correlation, with the Spearman coefficient  $r \sim 0.08$ . Figure 8(e) displays the relation between the T04 and Curti17 calibration metallicities, showing the Spearman coefficient  $r \sim 0.86$ . The relation between metallicities estimated by the Jon15 and Curti17 calibrators is shown in Figure 8(f), and their Spearman coefficient  $r \sim 0.34$  is exhibited. From Figures 8(e) and 8(f), we can see that T04 is a better calibrator than Jon15. Compared with Figures 8(a) and (e), we find that Curti17 is a better estimator than PP04. Therefore, we conclude

that Curti17 is the most accurate abundance indicator for composite ETGs out of the four metallicity calibrators.

Figure 9 displays the relation between SFR and  $12+\log(\text{O}/\text{H})$  for composite ETGs. Their metallicities are from four oxygen abundance indicators. Figure 9(a) describes the distribution of SFR and metallicity calibrated by the T04 estimator, and shows a trend that lower/higher SFR galaxies to have lower/higher metallicity. Here the correlation is not significant, and they have a Spearman coefficient  $r=0.44$ . This is not consistent with those found in Mannucci et al. (2010), showing that galaxies with a higher SFR tend to have lower metallicities at a fixed mass. Figure 9(b) demonstrates the relation between SFR and metallicity obtained by the Curti17 calibrator, and we can see the same rough trend as in Figure 9(a), by which a galaxy with lower/higher SFR has lower/higher metallicity. They present a weak Spearman coefficient of  $r=0.39$ .

The distribution of SFR and metallicity estimated by the Jon15 indicator is shown in Figure 9(c). The distribution does not present a correlation. The distribution of the PP04 calibration metallicity and SFR is displayed in Figure 9(d). We cannot see a significant tendency which has a similar positive correlation between the two parameters as in Figure 9(a), and they have a Spearman coefficient  $r=0.22$ . Therefore, the relation between SFR and metallicity calibrated by the Jon15 abundance indicator does not show a correlation, while the relation calibrated by the PP04, T04 and Curti17 indicators demonstrates a weak positive correlation. This indicates that a weak positive or no correlation between the SFR and metallicity is different from a negative correlation between both parameters in SFGs (Mannucci et al. 2010), and a weak correlation in the distribution of metallicity and SFR depends on the metallicity calibrated by different abundance indicators.

The weak positive correlation between SFR and metallicity indicates that some ETGs might have undergone recent gas-rich merger events. Since the low-level SF in local ETGs is driven by recent merger events, and most of these mergers do not involve a great deal of gas, dry major mergers or minor mergers are the candidates of these mergers (Kaviraj 2010). Major mergers are suggested to be too unusual to provide enough gas in the low-redshift universe, and they would possibly destroy stellar disks, while minor mergers are less violent events. The minor merger plays an important role in the local Universe (Kaviraj 2014), therefore mergers may be the dominant source of gas (Kaviraj et al. 2009, 2011; Davis et al. 2015; van de Voort et al. 2018).

From Figure 7, ETGs with a lower stellar mass often display lower SFRs, and these ETGs tend to have a smaller amount of interstellar matter (ISM) relative to massive ETGs, while minor merger with a lower mass companion can supply the gas, which has been accreted into the center of the galaxy, and it is easier for the inflow gas to dilute the metallicity of these ETGs than of massive ETGs. Combining the ISM property of ETGs and the dilution effect of merger-driven gas inflow, the weak correlation between SFR and  $12+\log(\text{O}/\text{H})$  is displayed in Figures 9(a), (b) and (d). Indeed, these minor mergers are not always gas rich (Davis et al. 2019), and they have different magnitudes of merger-induced metallicity dilu-

tion. Minor mergers dilute the metallicity of star-forming regions in ETGs, and can enhance the specific SFRs. van de Voort et al. (2018) used observations of six ETGs with the Atacama Large Millimeter/submillimeter Array, and found that this originates from a dynamical effect stabilizing the gas against gravitational collapse. So the enhancement of SFRs is less observed after merger-induced gas inflow in ETGs. In addition, the low-level SF efficiency is not enough to change the morphology of ETGs (Yildiz et al. 2015).

## 5. SUMMARY

In this study, the data of 9,739 ETGs were obtained by cross-matching the Galaxy Zoo 1 with our sample from the catalog of MPA-JHU emission-line measurements for the SDSS DR7. We first investigate the divisor between ETGs with and without SF with 77,476 ETGs. We then exclude various ionization sources to explore the ETG sample, and use the diagnostic tool of  $W2 - W3 = 2.0$  to derive our final sample. We utilize four abundance estimators to measure their metallicities. We summarize our main results as follows:

1. We investigate the separator between ETGs with and without SF, and employ a similar method of Herpich et al. (2016) to derive the best divisor of  $W2-W3=2.0$  color for ETGs.

2. We use the demarcation line of  $W2-W3=2.0$  to obtain a composite ETG sample by expanding the redshift range, and this diagnostic tool ( $W2-W3 > 2.0$ ) can select composite ETGs with SF. We derive the ETG sample of 5,376 galaxies, and estimate their metallicities by using four abundance indicators. Compared to the sample of Wu (2020), we have increased the sample size by 142%.

3. We show the main stellar mass range of  $10.0 < \log(M_*/M_\odot) < 11.5$  and the main sSFR range of  $-11.0 < \log(\text{sSFR}) < -9.5$ . Compared to the sample from Wu (2020), our median value of stellar masses increases from  $\log(M_*/M_\odot) = 10.58$  to 10.75, and their median values of sSFRs decrease slightly, from  $-10.34 \text{ yr}^{-1}$  to  $-10.50 \text{ yr}^{-1}$ .

4. We find that our composite ETG sample has a similar distribution of  $M_*$  and SFR to SFGs, and most of them lie on the “main sequence”. The fit of our data is  $\log(\text{SFR}) = (0.73 \pm 0.02)\log(M_*/M_\odot) - 7.61 \pm 0.19$ , and it is a slightly steeper slope than that derived in Renzini & Peng (2015), with  $0.76 \pm 0.01$ .

5. We compare the distribution of between different metallicities calibrated by four abundance indicators, and find that the Curti17 method is the most accurate calibrator for composite ETGs among the four abundance indicators.

6. We show that the distribution of SFR and metallicity, and find that a weak correlation only exists in the metallicity calibrated by the PP04, Curti17 and T04 indicators. The weak correlation is not consistent with the negative correlation of both parameters in SFGs, and the correlation depends on the metallicity calibrated by the abundance indicator. We suggest that the weak correlation may originate from the metallicity dilution of minor merger-driven gas inflow.

Y.-Z.W. thanks the anonymous referee for important comments and suggestions that improved the quality

of this paper significantly. This work is supported by

the Natural Science Foundation of China (NSFC; Nos. 11703044 and 12073047).

## REFERENCES

- Abazajian, K. N., Adelman-McCarthy, J. K., Agüeros, M. A. et al. 2009, *ApJS*, 182, 543
- Annibali, A., Bressan, A., Rampazzo, R., Zeilinger, W. W., Vega, O & Panuzzo, P. 2010, *A&A*, 519, 40
- Athey, A. E & Bregman, J. N. 2009, *ApJ*, 696, 681
- Baldwin, J. A., Phillips, M. M., & Terlevich, R. 1981, *PASP*, 93, 5
- Belfiore, F., Maiolino, R., Maraston, C., et al. 2016, *MNRAS*, 461, i3111
- Belli, S., Genzel, R., Forster Schreiber, N. M., et al. 2017, *ApJL*, 841, L6
- Blanton, M. R., Schlegel, D. J., Strauss, M. A., et al. 2005, *AJ*, 129, 2562
- Bresolin, F. 2013, *ApJL*, 772, L23
- Brown, J. S., Martini, P., Andrews, B. H. 2016, *MNRAS*, 458, 1529
- Caccianiga, A., Antón, S., Ballo, L., Foschini, L., Maccacaro, T., et al. 2015, *MNRAS*, 451, 1795
- Cattaneo, A., Faber, S. M., Binney, J., et al. 2009, *Nature*, 460, 213
- Chabrier, G. 2003, *PASP*, 115, 763
- Cid Fernandes, R., Stasińska, G., Mateus, A., et al. 2011, *MNRAS*, 413, 1687
- Cluver, M. E., Jarrett, T. H., Hopkins, A. M., et al. 2014, *ApJ*, 782, 90
- Curti, M., Cresci, G., annucci, F., Marconi, A., Maiolino, R., & Esposito, S. 2017, *MNRAS*, 465, 1384
- Davis, T. A., Rowlands, K., Allison, J. R., et al. 2015, *MNRAS*, 449, 3503
- Davis, T. A., Greene, J. E., Ma, C. P., et al. 2019, *MNRAS*, 486, 1404
- Emsellem, E., Cappellari, M., Krajnovic, D., et al. 2007, *MNRAS*, 379, 401
- Fang, J. J., Faber, S. M., Salim, S., Graves, G. J., & Rich, R. M. 2012, *ApJ*, 761, 23
- Geréb, K., Catinella, B., Cortese, L., Bekki, K., Moran, S. M & Schiminovich, D. 2016, *MNRAS*, 462, 382
- Griffith, E., Martini, P & Conroy, C. 2019, *MNRAS*, 484, 562
- Herpich, F., Mateus, A., Stasińska, G., Cid Fernandes, R., Vale Asari, N. 2016, *MNRAS*, 462, 1826
- Herpich, F., Stasińska, G., Mateus, A., Vale Asari, N., Cid Fernandes, R. 2018, *MNRAS*, 481, 1774
- Jones, T., Martin, C & Cooper, M. C. 2015, *ApJ*, 813, 126
- Kauffmann, G., Heckman, T. M., Tremonti, C., et al. 2003, *MNRAS*, 346, 1055
- Kaviraj, S. 2010, *MNRAS*, 408, 170
- Kaviraj, S. 2014, *MNRAS*, 437, L41
- Kaviraj, S., Sebastien, P., Khochfar, S., Silk, J & Kay, S. 2009, *MNRAS*, 394, 1713
- Kaviraj, S., Schawinski, K., Devriendt, J. E. G., et al. 2007, *ApJS*, 173, 619
- Kaviraj, S., Tan, K.-M., Ellis, R. S., & Silk, J. 2011, *MNRAS*, 411, 2148
- Kewley, L. J., Dopita, M. A., Sutherland, R., Heisler, C. A., & Trevena, J. 2001, *ApJ*, 556, 121
- Kewley, L. J., Grovers, B., Kauffmann, G., & Heckman, T. 2006, *MNRAS*, 372, 961
- Kroupa, P. 2001, *MNRAS*, 322, 231
- Kumari, N., Maiolino, R., Belfiore, F., & Curti, M. 2019, *MNRAS*, 485, 367
- Lintott, C. J., Schawinski, K., Bamford, S., Slosar, A., Land, K., et al. 2011, *MNRAS*, 410, 166
- Lintott, C. J., Schawinski, K., Slosar, A., Land, K., Bamford, S., et al. 2008, *MNRAS*, 389, 1179
- Mannucci, F., Cresci, G., Maiolino, R., Marconi, A., & Gnerucci, A. 2010, *MNRAS*, 408, 2115
- Martin, D. C., Fanson, J., Schiminovich, D., et al. 2005, *ApJL*, 619, L1
- Mateos, S., Alonso-Herreo, A., Carrera, F. J., et al. 2012, *MNRAS*, 426, 3271
- Mateus, A., Sodré, L., Cid Fernandes, R., et al. 2006, *MNRAS*, 370, 721
- Noeske, K. G., Weiner, B. J., Faber, S. M., et al. 2007, *ApJL*, 660, L43
- Pettini, M., & Pagel, B. E. J. 2004, *MNRAS*, 348, 59
- Renzini, A., & Peng, Y.-J. 2015, *ApJL*, 801, L29
- Salim, S., Rich, R. M., Charlot, S., et al. 2007, *ApJS*, 173, 267
- Schawinski, K., Lintott, C., Thomas, D., et al. 2009, *MNRAS*, 396, 818
- Shapiro, K. L., Falcón-Barroso, J., van de Ven, G., et al. 2010, *MNRAS*, 402, 2140
- Sparks, W. B., Macchetto, F., & Golombek, D. 1989, *ApJ*, 345, 153
- Stern, D., Assef, R. J., Benford, D. J., et al. 2012, *ApJ*, 753, 30
- Strateva, I., Ivezić, Ž., Knapp, G. R., et al. 2001, *AJ*, 122, 1861
- Tremonti, C. A., Heckman, T. M., Kauffmann, G., et al. 2004, *ApJ*, 613, 898
- van de Voort, F., Quataert, E., Faucher-Giguere, C., 2018, *MNRAS*, 476, 122
- Woods, T. E & Gilfanov, M. 2014, *MNRAS*, 439, 2351
- Wright, E. L., Eisenhardt, P. R. M., Mainzer, A. K., et al. 2010, *AJ*, 140, 1868
- Wu, Y.-Z., & Zhang, S.-N. 2013, *MNRAS*, 436, 934
- Wu, Y.-Z., Zhang, W., & Zhao, Y.-H.. 2019, *MNRAS*, 486, 5310
- Wu, Y.-Z. 2020, *ApJL*, 893, 33
- Yan, R. B. 2018, *MNRAS*, 481, 476
- Yi, S. K., Yoon, S.-J., Kaviraj, J.-M., Deharveng, R. M., Rich, R. M., et al. *ApJ*, 619, 111
- Yildiz, M. K., Serra, P., Oosterloo, T. A., et al. 2015, *MNRAS*, 451, 103